




Incommensurate spin ordering and excitations in multiferroic SrMnGe₂O₆

Claire V. Colin ^{1,*}, Lei Ding ², Eric Ressouche,³ Julien Robert,¹ Noriki Terada,⁴ Frederic Gay,¹ Pascal Lejay,¹ Virginie Simonet,¹ Céline Darie,¹ Pierre Bordet ¹ and Sylvain Petit⁵

¹Université Grenoble Alpes, CNRS, Institut Néel, 38000 Grenoble, France

²ISIS Facility, Rutherford Appleton Laboratory, Harwell Oxford, Didcot OX11 0QX, United Kingdom

³Université Grenoble Alpes, CEA, IRIG, MEM, MDN, F-38000 Grenoble, France

⁴National Institute for Materials Science, Sengen 1-2-1, Tsukuba, Ibaraki 305-0047, Japan

⁵Laboratoire Léon Brillouin, Université Paris-Saclay, CNRS, CEA, CEA-Saclay, Gif-sur-Yvette F-91191, France



(Received 23 December 2019; accepted 17 April 2020; published 2 June 2020)

Anisotropic multiferroic properties of SrMnGe₂O₆ pyroxene single crystals were systematically investigated by means of magnetization, heat capacity, pyroelectric current measurement, and elastic and inelastic neutron-scattering experiments. Single-crystal neutron diffraction allows us to unambiguously reveal the presence of two incommensurate magnetic orderings: a nonpolar amplitude-modulated collinear sinusoidal magnetic structure emerges at $T_{N1} = 4.36(2)$ K followed by a polar elliptical cycloidal spin structure below $T_{N2} = 4.05(2)$ K. Pyroelectric current measurements on single crystal confirm the appearance of a spontaneous polarization within the (*ac*) plane below T_{N2} associated with the latter magnetic symmetry through the extended Dzyaloshinskii-Moriya mechanism. The magnetic phase diagram was calculated considering the three isotropic exchange couplings relevant in this system. The magnetic excitations spectra of SrMnGe₂O₆ measured by inelastic neutron scattering were successfully modeled using a set of exchange interactions consistent with this phase diagram.

DOI: [10.1103/PhysRevB.101.235109](https://doi.org/10.1103/PhysRevB.101.235109)

I. INTRODUCTION

Strong coupling between magnetism and electricity in matter has become a central issue of condensed-matter physics from both fundamental and technological points of view. In so-called spin-driven multiferroics, an electric polarization emerges due to the symmetry breaking induced by the magnetic ordering. These last 15 years, a large variety of magnetic orderings was found to induce ferro- or ferrielectricity. Mainly three different microscopic models have been proposed to describe the observed ferroelectricity in different spin-driven ferroelectrics: for commensurate structures the relevant mechanism is exchange striction, whereas in incommensurate structures the inverse Dzyaloshinskii-Moriya (DM) model [1,2] is proposed for cycloid-type ordering, while a spin-dependent *p-d* hybridization model [3] is invoked in the proper screw type of magnetic ordering. The inverse DM model arising from the antisymmetric spin-exchange interaction between canted spin sites has been successfully used to explain the emergence of ferroelectricity in multiferroics with cycloidal order (like prototypical multiferroic TbMnO₃ [4]) but also transverse-conical spin order (for instance in spinel-type CoCr₂O₄ [5]). In addition, Kaplan and Mahanti [6] have shown that the extended inverse DM effect in some specific systems contributes to microscopic electric polarization in both cycloid and proper-screw helical systems.

Competing antiferromagnetic exchanges are well known to lead to frustration and give rise to modulated magnetic phases and rich phase diagram. It is the case in pyroxenes, which

are historically of great importance in mineralogy and have gained recent interest in condensed-matter physics because of the interplay between low dimensionality and magnetic frustration. The general formula of pyroxenes is AMX_2O_6 , where *A* is usually an alkali-metal ion with a valence of 1+ (e.g., Li⁺ and Na⁺) or an alkaline-earth ion with a valence of 2+ (Mg²⁺, Ca²⁺, and Sr²⁺), *M* refers to trivalent or divalent transition metal ions (e.g., Fe³⁺ and Mn²⁺), and *X* represents Si⁴⁺ or Ge⁴⁺. Based on the observation of electric polarization under magnetic fields, Jodlauk *et al.* [7] reported that the clinopyroxene (pyroxene with a monoclinic crystal structure) compounds NaFeSi₂O₆, LiFeSi₂O₆, and LiCrSi₂O₆ could display multiferroism. They suggested that the quasi-one-dimensional spin chain of M^{3+} ions should be subject to spin frustration between intrachain and interchain interactions resulting in an incommensurate spin structure. These magnetic structures could induce ferroelectric polarization, possibly due to the formation of spiral spin ordering. Subsequent neutron diffraction and electric polarization studies revealed that not only NaFeSi₂O₆ [8–10] but also NaFeGe₂O₆ [9,11–14] are spin driven multiferroics, while LiFeSi₂O₆ [15,16], LiCrSi₂O₆ [17–19], and also CaMnGe₂O₆ [20] are linear magnetoelectric materials. In pyroxene triangular topology, the $3d^5$ electronic configuration of the transition metal is a crucial feature to trigger magnetic frustration because it is the only one that gives rise to predominant and uniform antiferromagnetic (AFM) interactions along the octahedra chains [21]. Recently, we have established that the divalent pyroxene SrMnGe₂O₆, with Mn²⁺ in a $3d^5$ electronic configuration, presents indeed multiferroism [22].

The structure of SrMnGe₂O₆, [$C2/c$, $a = 10.346(2)$ Å, $b = 9.420(2)$ Å, $c = 5.511(1)$ Å, $\beta = 104.669(5)$] shown in

*claire.colin@neel.cnrs.fr

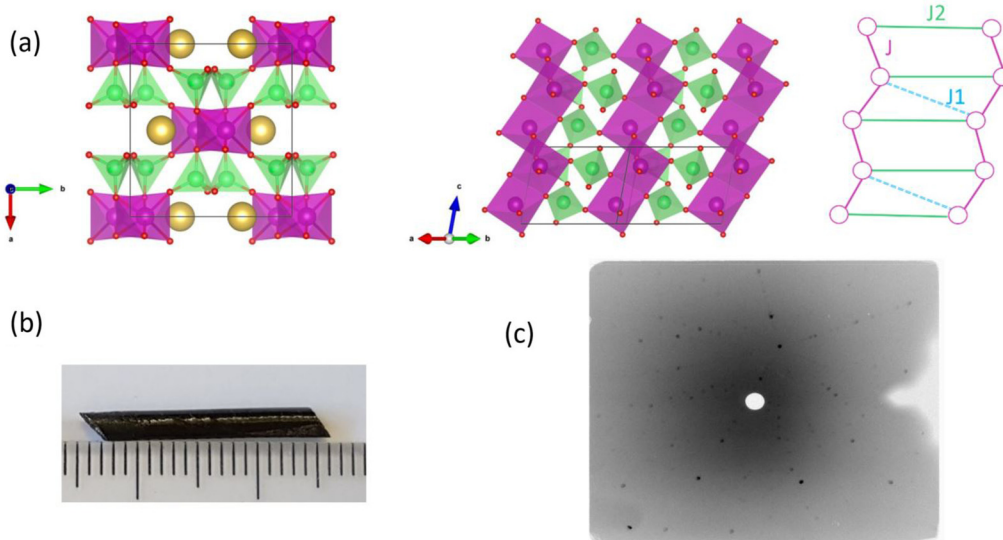


FIG. 1. (a) Crystal structure of $\text{SrMnGe}_2\text{O}_6$ ($C2/c$) projected along two different directions. Atoms are represented by colored spheres: Sr in gold, Mn in purple, Ge in green, and O in red. Right: Sketch of the three main exchange interactions. (b) Photograph and (c) x-ray Laue image of the single crystal of $\text{SrMnGe}_2\text{O}_6$ grown by floating zone method.

Fig. 1(a), is characterized by zigzag spin chains of Mn^{2+} running along the c axis. Along the a axis, the spin chains are connected via GeO_4 tetrahedra, and thus intrachain interaction (J) along the c axis is strongest while the weaker interchain interactions (J_1 and J_2) can be a source of competing spin interactions. Therefore, the magnetic arrangement can be regarded as a spin-frustrated network of quasi-one-dimensional spin chains, thus prone to the formation of incommensurate spin ordering.

Recently, we have succeeded in growing a large single crystal of $\text{SrMnGe}_2\text{O}_6$ by the floating zone furnace technique, as can be observed in Fig. 1(b). In the present study, we extend the investigation done previously on powders [22] by using these single crystals and access the anisotropic properties. Hereafter are reported our single-crystal magnetization, heat capacity, pyroelectric current measurements, as well as elastic and inelastic neutron-scattering experiments.

II. EXPERIMENTAL DETAILS

Single crystals of $\text{SrMnGe}_2\text{O}_6$ were grown using the floating zone furnace technique. To prepare $\text{SrMnGe}_2\text{O}_6$ powders the starting materials of reagent-grade SrCO_3 , MnO_2 , and GeO_2 were thoroughly ground in an agate mortar and pressed into pellets. The pellets were placed in a platinum boat and heated in air to 1100°C at $100^\circ\text{C}/\text{h}$, then held at 1100°C for 10 days and cooled down to room temperature. The powder was sealed in a rubber tube, evacuated, and compacted into a rod (typically 4 mm in diameter and 10 cm long) using a hydraulic press under an isostatic pressure of 1 GPa. After removal from the rubber tube, the rods were sintered at 1100°C for 5 days in air. Single crystals of approximately 4 mm in diameter and up to 50 mm in length were grown from the polycrystalline feed rods in a floating zone furnace. Growths were carried out under air at room pressure. The crystal growth rate was maintained at 4 mm/hr. Samples with dimensions suitable for the particular measurements and with

different crystallographic orientations were cut from the same crystal. Both x-ray and neutron single-crystal Laue diffraction confirmed the good crystallinity of the as-grown single crystals.

Magnetization was measured using a superconducting quantum interference device detection magnetometer (MPMS-XL by Quantum Design). The dc magnetic susceptibility measurements were performed under both zero-field-cooled (ZFC) and field-cooled (FC) procedures over the temperature range between 2 and 300 K in a magnetic field of 0.1 T.

Heat-capacity measurement was carried out using a relaxation technique on a Quantum Design Physical Property Measurement System (PPMS). A small single crystal was mounted on a sample platform with Apiezon N grease for better thermal contact. The heat capacity was recorded in the temperature range of 2–300 K without external field.

The temperature dependence of electric polarization of $\text{SrMnGe}_2\text{O}_6$ was obtained by the pyroelectric current method. The oriented single crystals were coated with silver epoxy on both parallel surfaces of the sample. A poling field, E_p , up to ± 500 kV/m was first applied in the paraelectric state at temperature 6–10 K prior to cooling the sample through the Néel temperature down to 2 K in order to obtain a single polar domain state. At 2 K, the poling field was removed. Then, the sample was heated at a constant rate of 3 K/min, and the pyroelectric current curves were recorded using a Keithley 6514 electrometer. Electric polarization curves were eventually obtained by the integration of the time dependence of the observed pyroelectric current.

Neutron-diffraction experiments were carried out on the CEA-CRG D23 4-circle single-crystal diffractometer at the Institut Laue Langevin (Grenoble, France) with an incident wavelength $\lambda = 1.277 \text{ \AA}$ selected by a fixed curvature Cu 200 monochromator. The single crystal was mounted in a close-cycle refrigerator and data collections were carried out at several temperatures in the paramagnetic domain and for

each of the magnetic phases. The refinements were done using the FULLPROF suite package [23] by least-squares refinements using the integrated intensities and including an extinction correction following the model of Becker and Coppens [24]. To refine the magnetic structures, the crystallographic parameters and the scale factors were fixed to the values obtained in the crystalline refinements. The spin configurations have been described as follows: for a given magnetic propagation vector \mathbf{k} (and the associated $-\mathbf{k}$),

$$\begin{aligned} \mathbf{m}_{lj} = & m_{1j} \hat{u}_j \cos[2\pi(\mathbf{k} \cdot \mathbf{R}_l + \Phi_j)] \\ & + m_{2j} \hat{v}_j \sin[2\pi(\mathbf{k} \cdot \mathbf{R}_l + \Phi_j)], \end{aligned} \quad (1)$$

where \mathbf{m}_{lj} is the magnetic moment of the atom j in the unit cell l , \mathbf{R}_l is the vector joining the arbitrary origin to the origin of unit cell l , and Φ_j is a magnetic phase. Group-theoretical calculations were done using ISODISTORT [25] and Bilbao crystallographic server (magnetic symmetry and application [26]) software.

The inelastic neutron scattering (INS) experiment was carried out on the 4F2 cold neutron three-axis spectrometer at the Laboratoire Léon Brillouin (ORPHÉE Reactor, Saclay, France). The spectrometer was equipped with focusing Pyrolytic Graphite PG (002) monochromator and analyzer. A Be filter was implemented in the scattered beam to remove high-order contaminations. The final energy E_f was set to 4.9 or 3.48 meV ($K_f = 1.55$ and 1.3 \AA^{-1} , yielding an energy resolution of about 0.22 and 0.1 meV respectively). The INS measurement was performed on a long single crystal ($21 \times 2 \times 2 \text{ mm}^3$, 176 mg). The sample was mounted on a standard orange cryostat, and aligned in the $(0 \text{ K } L)$ scattering plane.

III. RESULTS

A. Magnetic and multiferroic properties

Temperature dependence of the magnetic susceptibility curves under a magnetic field along the a , b , and c^* axes of $\text{SrMnGe}_2\text{O}_6$ are shown in Fig. 2(a). The anomalies in these curves indicate the presence of two successive magnetic transitions. At $T_{N1} = 4.36 \text{ K}$, the first magnetic transition is clearly visible by a drop in the magnetic susceptibility along the a direction while only a small kink is observed along the b and c^* directions. The second magnetic phase transition is featured by a sudden drop in the susceptibility along the b axis at $T_{N2} = 4.05 \text{ K}$ [Fig. 2(b)]. The two successive magnetic transitions can be further confirmed by heat-capacity measurements. As shown in Fig. 2(b), the specific-heat curve exhibits a sharp peak and a lambda-like anomaly at $T_{N1} = 4.36(2) \text{ K}$ and $T_{N2} = 4.05(2) \text{ K}$, respectively, coinciding with the two magnetic transitions. Only one magnetic phase transition was observed in our previous study on powder, probably because the two transitions are very close in temperature.

The electric polarization anisotropy measured on a single crystal often provides insights in the understanding of the pertinent mechanisms of multiferroicity. We have performed pyroelectric current measurements with the poling electric field applied along the a , b , and c^* directions under $Ep = 500 \text{ kV m}^{-1}$. As shown in Fig. 3, the spontaneous electric polarization develops very close to 4 K and increases with decreasing temperature to reach $\sim 3 \mu\text{C m}^{-2}$ at 2 K along

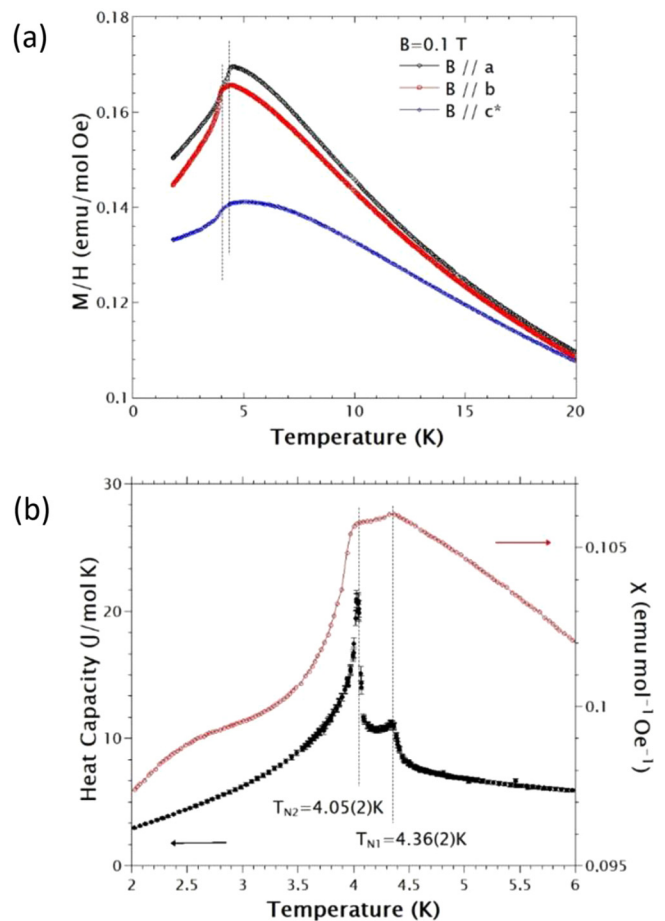


FIG. 2. (a) Temperature dependence of magnetic susceptibility measured under a magnetic field of 0.1 T applied along the a , b , and c^* axis. (b) Temperature dependence of heat capacity and magnetic susceptibility measured under a magnetic field of 0.01 T applied along the b axis. The dashed lines indicate magnetic phase transitions.

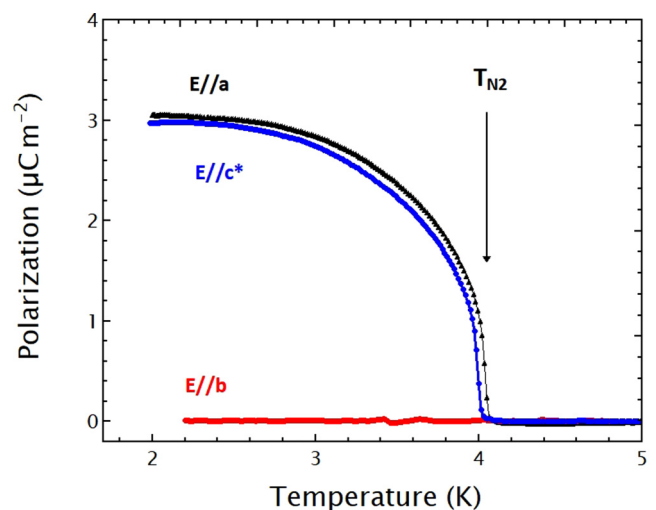


FIG. 3. Temperature dependence of the electric polarization of $\text{SrMnGe}_2\text{O}_6$ measured with the electric field parallel to the a , b , and c^* axis.

TABLE I. Agreement factors and refined structural parameters for SrMnGe₂O₆ at 2 K. The average distance, octahedral distortion, and effective coordination number are also given for MnO₆ octahedron.

Name	x	y	z	$B(\text{\AA}^2)$
Sr	0	0.308 55(13)	0.25	0.303(28)
Mn	0	0.907 60(23)	0.25	0.072(42)
Ge	0.282 44(6)	0.095 46(8)	0.219 27(13)	0.169(24)
O1	0.111 07(9)	0.087 42(11)	0.139 57(19)	0.344(28)
O2	0.357 83(10)	0.254 69(11)	0.318 08(21)	0.394(25)
O3	0.353 51(8)	0.021 79(11)	0.981 19(20)	0.312(28)

Mn-O1-Mn = 96.12(6)^o
Mn-Mn distance through J : $d = 3.257(3)$ \AA
Mn-Mn distance through J_1 : $d_1 = 5.996(2)$ \AA
Mn-Mn distance through J_2 : $d_2 = 6.9896(19)$ \AA

MnO₆ octahedron:
Average bond length = 2.1784 \AA
Distortion index (bond length) = 0.01072
Effective coordination number = 5.9725

Space group $C2/c$; $a = 10.3559$ \AA, $b = 9.3903$ \AA, $c = 5.5133$ \AA, $\beta = 104.651^\circ$, $R_{F2} = 4.59$, $R_{F2w} = 6.26$, $R_F = 2.62$, $\chi^2 = 118$.
Number of reflections: 582.

the a and c^* directions. On the other hand, there is minimal or no polarization seen along the b direction. The electric polarization value changes its sign with reversal of the electric poling direction which directly evidences that SrMnGe₂O₆ is indeed ferroelectric below 4 K. Moreover, the concomitant ferroelectric and antiferromagnetic transition at $T_{N2} = 4.05$ K confirms that SrMnGe₂O₆ is a multiferroic compound, while the magnetic ordering at $T_{N1} = 4.36$ K does not seem to cause a ferroelectric order.

B. Neutron diffraction

The structural refinement based on single-crystal neutron-diffraction data confirmed that SrMnGe₂O₆ crystallizes with the $C2/c$ symmetry, in good agreement with our previous results based on single-crystal x-ray-diffraction data [22]. No structural phase transition could be detected by our temperature-dependent neutron-diffraction measurements down to 2 K. The atomic coordinates, displacement parameters, and principal structural parameters are given in Table I. Although the Mn-O1-Mn in-chain bond angle departs from 90^o [Mn-O1-Mn = 96.12(6)^o], the oxygen octahedra surrounding the Mn²⁺ cations remain very regular as reflected by the small value of the distortion index based on bond lengths, D , defined by Baur [27].

Single-crystal neutron-diffraction experiments show that magnetic Bragg reflections appear below T_{N1} ($ICM1$ phase) which can be indexed by an incommensurate propagation vector $\mathbf{k} = (0, k_y, 0)$ with $k_y = 0.381(1)$ at 4.1 K. In Fig. 4, one can clearly see that the modulus of the k vector increases significantly below T_{N2} to reach $k_y = 0.425(1)$ at 2 K, which marks the transition to the lower temperature $ICM2$ phase. This transition is also reflected by a kink in the evolution of the integrated intensity of $(1, 1-k_y, 1)$ reflection. The k vector corresponding to the $ICM2$ phase is consistent with the one previously observed by neutron powder diffraction [22]. To determine the magnetic structures, 248 reflections belonging to the $ICM1$ phase were collected at 4 K and 290 reflections

were collected at 2 K for the $ICM2$ phase. Possible magnetic models were searched using the simulated annealing method and the corresponding magnetic structures were then refined. The two orbits Mn1 (0, 0.90760, 0.25) and Mn2 (0, 0.09240, 0.75) were constrained to have the same magnetic moment. Only the magnetic phase difference $\Delta\Phi$ between these two sites was refined. The parameters that describe the proposed spin arrangements are gathered in Table II.

The magnetic structure in the $ICM1$ phase was determined as an amplitude-modulated collinear sinusoidal structure with the reliability factor $R_f = 11\%$. The refinement leads to a magnetic moment of $1.961(6)\mu_B$ along the easy-magnetic axis [Fig. 5(a)]. As shown in Fig. 5(c), the easy-magnetic axis is confined into the (ac) plane but with an

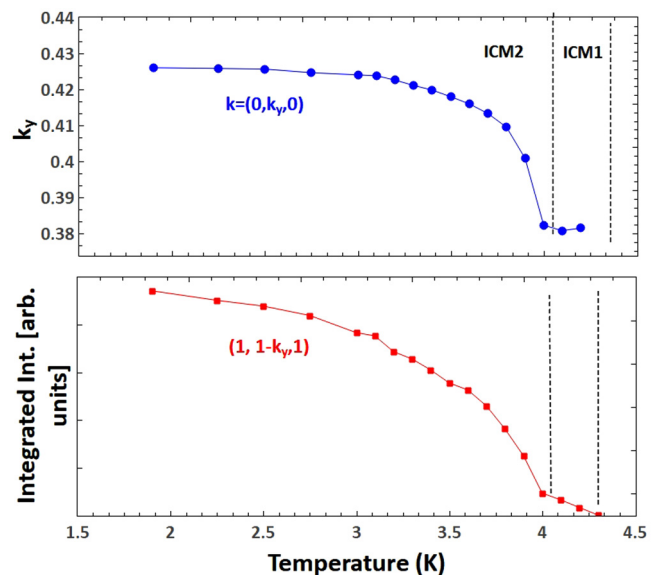


FIG. 4. Temperature dependence of the k_y component of the magnetic propagation vector $\mathbf{k} = (0, k_y, 0)$ (top) and the integrated intensity of the $(1, 1-k_y, 1)$ magnetic reflection (bottom).

TABLE II. Refined parameters of SrMnGe₂O₆ magnetic structures at 2 and 4.1 K under zero field. Both structures have a propagation vector of the form $k = [0, k_y, 0]$. The unitary vectors \hat{u} and \hat{v} are described by spherical angles: φ is the angle that the projections of the unitary vectors in the xy plane make with x ($\parallel a$) and θ is the angle the unitary vectors make with z ($\parallel c$). $\Delta\Phi$ corresponds to the magnetic phase difference of Mn1 (0, 0.90760, 0.25) and Mn2(0, 0.09240, 0.75). α is the angle between the plane where the moments lie and a direction in the ac plane. m_{1j} and m_{2j} correspond to the modulus of the orthogonal components of magnetic moments. R_{F2} , R_{F2w} , R_F , and χ^2 are the reliability factors.

Temperature		2 K	4.1 K
Magnetic superspace group		$Bb1'(0, 0, g)0s$	$B2/b1'(0, 0, g)s0s$
Basis		$(-1, 0, 0, 0, 0, -1, 0, 0, -1, 0, 0, 0, 0, 1)$	$(-1, 0, 0, 0, 0, 0, -1, 0, 0, -1, 0, 0, 0, 0, 1)$
Propagation vector		$[0, k_y, 0]$	$[0, k_y, 0]$
k_y		0.425	0.381
Mn1, Mn2	$m_{1j}(\mu_B)$	4.26(2)	1.961(6)
	φ_u	0°	0
	θ_u	71.4(3)°	71.5(4)
	$m_{2j}(\mu_B)$	3.90(2)	
	φ_v	90°	
	θ_v	90°	
$\Delta\Phi$		0.1744(6)	0.2089(15)
α		18.6(3)°	18.5(4)°
$R_{F2}(\%)$		4.37	12.5
$R_{F2w}(\%)$		4.79	10.2
$R_F(\%)$		3.54	11.0
χ^2		3.79	2.73
Number of reflections		290	248

angle of $\alpha = 18.5^\circ$ away from the a axis towards the c axis. The corresponding magnetic superspace group of the *ICM1* phase is $B2/b1'(0, 0, g)s0s$ with $g = k_y$ [25,28], generated by the single magnetic irreducible representation *mLD2* (see Table III). Such magnetic symmetry preserves the twofold

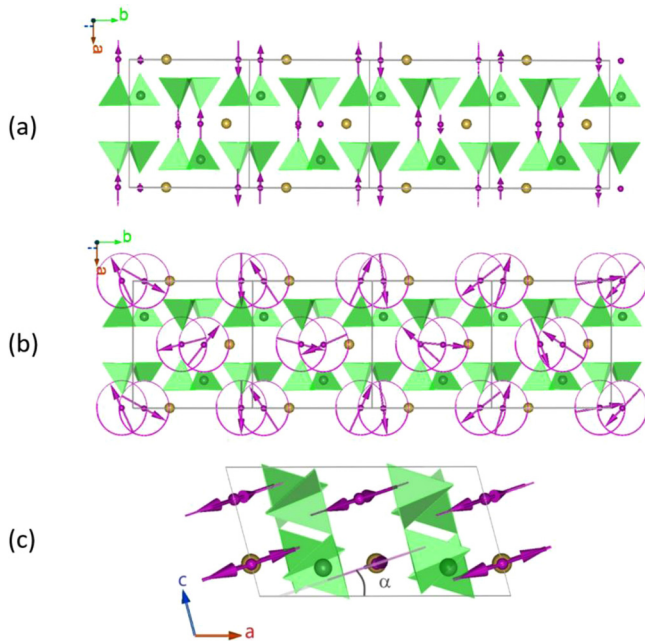


FIG. 5. Illustration of the determined magnetic structures: (a) *ICM1* amplitude-modulated collinear sinusoidal structure with moments along the direction defined by the α angle (b) *ICM2* elliptical cycloidal spin structure with the moments rotating within the ab plane (c) α angle give the direction of the easy magnetic axis located at about 18.5° from the a axis towards the c axis.

axis and the mirror plane symmetry, resulting in the centrosymmetric magnetic point group $2/m1'$. This explains the absence of spontaneous electric polarization between T_{N1} and T_{N2} .

The determination of the magnetic structure of the *ICM2* phase (reliability factor $R_f = 3.54\%$) leads to an elliptical cycloidal spin structure with the moments rotating within the plane formed by the b axis and the same easy-magnetic axis than in *ICM1* phase [cf. Figs. 5(a) and 5(c)]. It is worth noticing that the moments are close to being perpendicular to the c direction (4° off). Tentative refinements constraining them to be exactly normal to the c direction lead however to a much lower fit quality. At 2 K, the refined Mn²⁺ magnetic moment varies from $4.26(2)\mu_B$ along the long axis of the ellipse to $3.90(2)\mu_B$ along the short axis. The magnetic superspace group describing this magnetic structure is $Bb1'(0, 0, g)0s$ where two magnetic irreducible representations *mLD1* and *mLD2* have to be combined to generate the magnetic structure. It breaks the structural twofold axis and keeps the mirror plane symmetry perpendicular to the unique b axis, leading to the polar magnetic point group $m1'$. The corresponding magnetic

TABLE III. Nonzero IR's and associated basis vectors ψ for the space group $C2/c$ with $k = [0, 0.424, 0]$. The magnetic atoms Mn²⁺ at 4e site are split into two independent orbits: Mn1 (0, 0.90760, 0.25) and Mn2 (0, 0.09240, 0.75).

IR	Basis vector	Orbit 1			Orbit 2		
		m_x	m_y	m_z	m_x	m_y	m_z
<i>mLD1</i>	$\psi 1$	0	1	0	0	1	0
<i>mLD2</i>	$\psi 2$	1	0	0	1	0	0
	$\psi 3$	0	0	1	0	0	1

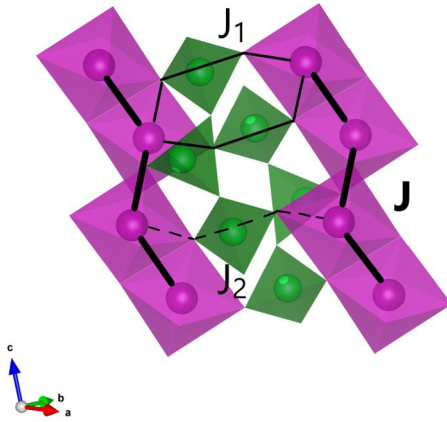


FIG. 6. The MnO_6 zigzag chains connected through GeO_4 tetrahedra in $\text{SrMnGe}_2\text{O}_6$. The bold solid, thin solid, and dotted lines correspond to exchange paths J , J_1 , and J_2 .

point group allows the existence of spontaneous polarization in any direction perpendicular to the mirror, i.e., in the (ac) plane, in good agreement with the observed spontaneous polarization along a and c^* (Fig. 3).

C. Magnetic phase diagram

As explained above the dominant magnetic interaction (J) between the Mn^{2+} nearest-neighbor cations ($d = 3.257 \text{ \AA}$) along the octahedra chains is mediated by superexchange interactions through the O1 oxygen anion in competition with direct exchange interactions. The magnetic coupling between MnO_6 chains is operated through the bridging GeO_4 tetrahedra (see Fig. 6). Two magnetic interactions J_1 and J_2 are expected to play an important role for diverse magnetic orderings: J_1 is governed by a double supersuperexchange (SSE) path through edges of two different GeO_4 tetrahedra ($d_1 = 5.996 \text{ \AA}$), while J_2 is given by a single SSE at a longer distance ($d_2 = 6.989 \text{ \AA}$).

This model with the three isotropic [29] exchange interactions (J , J_1 , J_2) was solved assuming classical spins to determine the ordered spin configurations in $\text{SrMnGe}_2\text{O}_6$. The Luttinger-Tisza method [30] was used for finding the ordering wave-vector q_0 that minimizes the total classical energy $E(\mathbf{q}) = -N|\mathbf{S}(\mathbf{q})|^2 \lambda_0(\mathbf{q})$ [with N the number of spins and $\mathbf{S}(\mathbf{q})$ their Fourier components], i.e., that maximizes the highest eigenvalue $\lambda_0(\mathbf{q})$ of the Fourier transform of the interaction matrix $\mathbf{J}(\mathbf{q})$, for given sets of exchange couplings J , J_1 , J_2 . The resulting classical phase diagram in the $(J_1/|J|, J_2/|J|)$ is represented in Fig. 7. When one of the interchain interactions dominates the other, commensurate orders are found: J_1 promotes $\mathbf{k} = 0$ while J_2 tends to break the centering C with a $\mathbf{k} = (0, 1, 0)$ vector. The $\mathbf{k} = 0$ commensurate order is found in most of the pyroxenes with the same crystal structure of space group $C2/c$ with AFM J , in $\text{NaCrGe}_2\text{O}_6$ [31], $\text{NaCrSi}_2\text{O}_6$ [32], and $\text{CaMnGe}_2\text{O}_6$ [20]. Incommensurate order comes out from the competition between J_1 and J_2 interchain interactions; it represents a large intermediate sector of the phase diagram. The stabilized incommensurate k vector is $(0, k_y, 0)$. It is worth noticing that in some part of the diagram $(k_x, 0, k_z)$ order is very close in energy and may be further stabilized by introducing a small antiferromag-

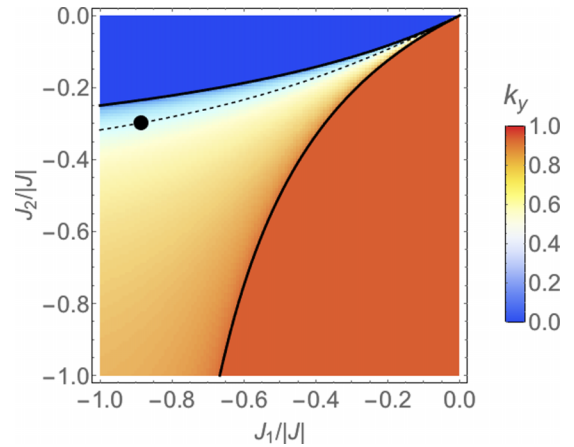


FIG. 7. Magnetic phase diagram for an antiferromagnetic intrachain interaction $J < 0$, representing the stability of different magnetic ground states in function of on relative values of the exchange parameters, $J_1/|J|$ and $J_2/|J|$. Phase boundaries are represented by the plain black lines while the dashed one shows the iso $-k_y = 0.424$. The black point is the sets of parameters obtained for $\text{SrMnGe}_2\text{O}_6$ (see text). The color scale represents the k_y value: the red region shows the magnetic phase characterized by $k = (0, 1, 0)$, while the region in blue corresponds to the $k = 0$ phase.

netic next-nearest-neighbor (NNN) interaction in the chain. This is probably the case with $\text{NaFeGe}_2\text{O}_6$ [14]. Note that $\mathbf{k} = (0, 1, 0)$ is found in all pyroxenes where the intrachain interaction is ferromagnetic: $\text{CaM}(\text{Si}, \text{Ge})_2\text{O}_6$ with $M = \text{Fe}, \text{Co}, \text{Ni}$ [33] and $\text{SrCoGe}_2\text{O}_6$ [22].

To get more insight into the phase diagram, we have also calculated analytically the classical energy for the $\mathbf{k} = (0, k_y, 0)$ propagation vector. Minimizing the classical energy with respect to k_y leads to the following relation between k_y and the exchange interactions J_1 and J_2 :

$$J_2 = \frac{J_1}{2\sqrt{J^2 + 2J_1 \cos(k_y/2) + J_1^2}} \quad (2)$$

for J_1 and $J_2 < 0$ (AFM). The line displayed on Fig. 7 illustrates this relationship for $k_y = 0.424$. Taking into account the phase ($\Delta\Phi$) between the magnetic moment directions of the two magnetic sites gives another parametrization:

$$\frac{J_1}{|J|} = -\frac{\sin(k_y + \Delta\Phi)}{\sin\left(\frac{k_y}{2} + \Delta\Phi\right)},$$

$$\frac{J_2}{|J|} = -\frac{\sin(k_y + \Delta\Phi)}{2 \sin\left(\frac{k_y}{2}\right)}.$$

If we now consider the actual structure refined in $\text{SrMnGe}_2\text{O}_6$ at 2 K [$k_y = 0.424(1)$, $\Delta\Phi = 62.8(2)^\circ$], it gives $J_1/|J| = 0.88(2)$ and $J_2/|J| = 0.29(1)$ which is represented by the black point marked in Fig. 7.

D. Spin-wave excitations from inelastic neutron scattering

To cross check this analysis, we have carried out an inelastic neutron-scattering (INS) experiment at 2 K. Representative raw data scans are shown in Fig. 8.

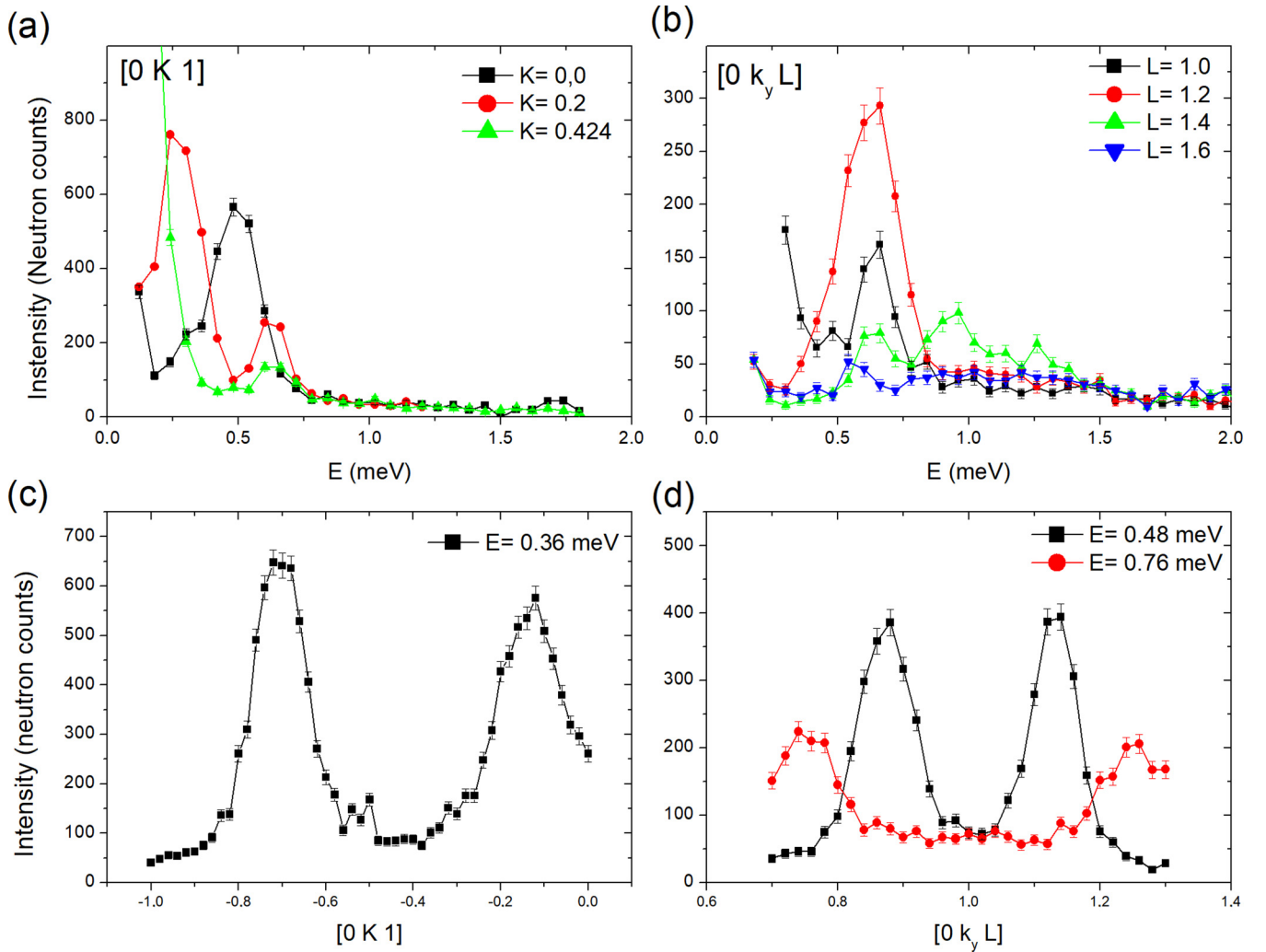


FIG. 8. Energy scans measured at selected positions $Q = (0K1)$ (a) and $Q = (0k_yL)$ (b) to determine the magnon dispersion in the ferroelectric elliptical cycloidal phase at $T = 1.5$ K. (c), (d) Representative Q scans at constant energy transfer in the $[0K1]$ (c) and $[0k_yL]$ (d) directions crossing the spin-wave excitations.

Well-defined spin-wave excitations are observed, as shown also in Fig. 9. Acoustic modes emerge from the incommensurate $(0, k_y, 1)$ Bragg peaks and disperse throughout the Brillouin zone up to about 1 meV, as expected in such a noncollinear structure. Along L , a more complicated spectrum emerges: the acoustic modes go soft at integer $L = 1$ and 2, while an optical mode is also observed at about 0.7 meV.

To model the spin dynamics, spin-wave calculations were performed using the SPINWAVE software [34] developed at Laboratoire Léon Brillouin (LLB). The Hamiltonian governing the magnetic properties is of the form

$$\begin{aligned}
 H = & J \sum_{i,j}^{\text{in chain}} S_i S_j + J_1 \sum_{i,j}^{\text{inter chain}} S_i S_j \\
 & + J_2 \sum_{i,j}^{\text{inter chain}} S_i S_j + \sum_i B_{i,20} \vartheta_{i,20}.
 \end{aligned}$$

In addition to the J , J_1 , and J_2 terms, a single-ion anisotropy term was taken into account, modeled by $V = 3/2 B_{20} S_{z,i}^2$. Here B_{20} is positive to ensure that the spins lie in the easy

plane and stabilize the cycloid structure, as inferred from diffraction. Diagonalization of the Hamiltonian in the spin-wave approximation allows us to calculate the spin-spin correlation function as observed by inelastic neutron-scattering experiments. As we have seen before, considering the actual structure refined in $\text{SrMnGe}_2\text{O}_6$ gives constraints on the ratios $J_1/|J|$ and $J_2/|J|$ to fulfill Eq. (2). The values of J and B_{20} have yet to be determined. To this end, we have carried out a series of calculations keeping the ratios $J_1/|J|$ and $J_2/|J|$ constant, but varying J and B_{20} in a systematic way. The detailed study is presented in the Appendix. The best reasonable agreement is found for the following set of interactions consistent with the refined magnetic structure, i.e., $J = 0.11(1)$ meV, $J_1 = 0.086(12)$ meV, and $J_2 = 0.031(4)$ meV, and $B_{20} = 0.12(3)$ meV, see Fig. 9, hence showing the consistency of this analysis against our neutron results.

IV. DISCUSSION

We have just seen that the refined magnetic structure, the calculated magnetic phase diagram, and the spin

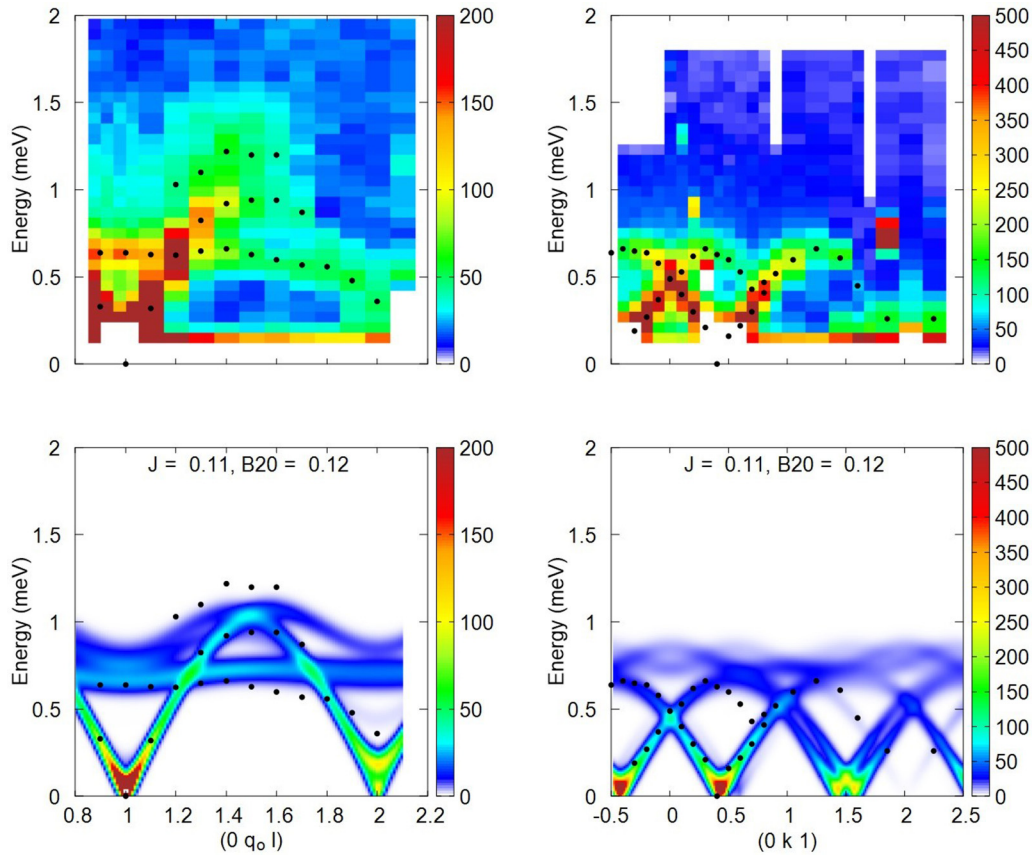


FIG. 9. Measured (top) and calculated (bottom) intensity mapping of the inelastic intensity for $T = 2$ K along $Q = (0ky1)$ and $(0k1)$ direction; black circles mark the fitted magnon energies. The calculations were performed with $J = 0.11$ meV, $J_1 = 0.086$ meV and $J_2 = 0.031$ meV and planar single-ion anisotropy = 0.12 meV.

wave measured in $\text{SrMnGe}_2\text{O}_6$ are well captured by the simple model of three isotropic exchange interactions J , J_1 , and J_2 . This study shows the experimental determination of exchange interactions done on pyroxene compounds. DFT calculations were however performed on isostructural compounds with $3d^5$ magnetic cation: $\text{CaMnGe}_2\text{O}_6$ [35] and $\text{NaFeGe}_2\text{O}_6$ [14]. The hierarchy and the sign of the exchange interactions is the same in the three compounds: all interactions are antiferromagnetic and the strongest is the exchange interaction along the chains (superexchange J), while the second largest exchange coupling is via the two GeO_4 tetrahedra [supersuperexchange (SSE) J_1]. This hierarchy can be explained by (i) the nature of the interaction SE vs SSE, (ii) the Mn-Mn distances, and (iii) the fact that J_1 involves two GeO_4 bridges compared to only one for J_2 . $\text{SrMnGe}_2\text{O}_6$ has much weaker exchange interaction values than in the other two compounds ($J_{\text{NaFeGe}_2\text{O}_6} = 12.3$ K, $J_{\text{CaMnGe}_2\text{O}_6} = 3.6$ K, $J_{\text{SrMnGe}_2\text{O}_6} = 1.04$ K), which is reflected also in the Néel ordering temperatures ($T_{\text{N NaFeGe}_2\text{O}_6} = 13$ K, $T_{\text{N CaMnGe}_2\text{O}_6} = 15$ K, $T_{\text{N SrMnGe}_2\text{O}_6} = 4.36$ K). The weaker exchange interaction in $\text{SrMnGe}_2\text{O}_6$ can be understood by considering the distortion of the ideal pyroxene structure due to the large Sr^{2+} cation size. First of all, in $\text{SrMnGe}_2\text{O}_6$ the magnetic cation distances $M-M$ in between the chains (d_1-J_1 and d_2-J_2) are much larger than in $\text{NaFeGe}_2\text{O}_6$ (for instance $d_1 = 5.996$ Å in $\text{SrMnGe}_2\text{O}_6$ with respect to 5.64 Å in $\text{NaFeGe}_2\text{O}_6$ [9]). Then, let us consider the strength of the

dominant intrachain magnetic interaction J in $\text{SrMnGe}_2\text{O}_6$. Superexchange through the O1 oxygen anion between the Mn^{2+} nearest-neighbor cations along the octahedra chains is in competition with direct exchange. The detailed analysis of the different orbital contribution done by Streltsov and Khomskii [21] show that the $t_{2g}-e_g$ contribution is the strongest and is AFM. e_g-e_g orbitals give a smaller contribution but which is subtly dependent on the angle $M-O-M$. For an angle close to 90° the FM contribution dominates, while it is outbalanced by AFM for a much larger angle, the compensation occurring at about 97° . In $\text{SrMnGe}_2\text{O}_6$, the angle $M-O1-M$ is $96.12(6)^\circ$, close to the compensation angle, and therefore e_g-e_g orbitals have low or no contribution. In $\text{NaFeGe}_2\text{O}_6$ however, the $M-O-M$ angle is $\sim 102.7^\circ$ and the e_g-e_g contribution reinforces the AFM character of the interaction. This is an important difference between the compounds because while for $\text{NaFeGe}_2\text{O}_6$ [14] the value of intrachain J is nearly three times larger than interchain interactions J , in $\text{SrMnGe}_2\text{O}_6$ J and J_1 are comparable ($J_1/J = 0.88$). This raises the question of whether $\text{NaFeGe}_2\text{O}_6$ is in the quasi-one-dimensional limit unlike $\text{SrMnGe}_2\text{O}_6$. This is a nontrivial issue because the connectivity is quite peculiar in pyroxenes. While J connects the spins of a given chain running along the c axis, J_1 connects two spins alternately within the neighboring left, right, front, and back chains. In this sense, even with J and J_1 comparable, $\text{SrMnGe}_2\text{O}_6$ is not fully three dimensional.

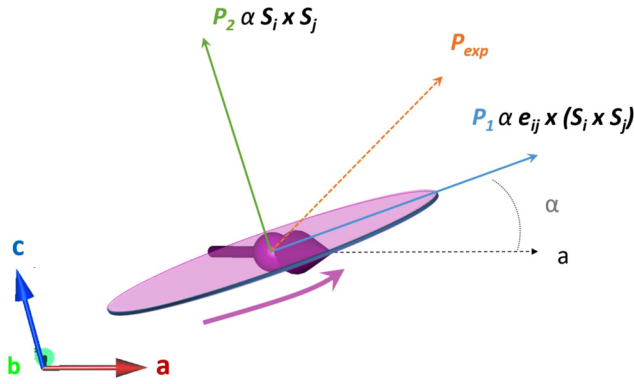


FIG. 10. Schematic illustration representing the elliptical cycloid running along the b axis and the electric polarization directions in the (a, c) plane, P_{exp} being the experimental one, P_1 and P_2 corresponding to the extended inverse DM mechanism [6].

Several experimental facts evidence that magnetic anisotropy is an important feature in $\text{SrMnGe}_2\text{O}_6$. First, the magnetization susceptibility measured along the c^* direction is much smaller than along b and a , which is consistent with c^* being a hard axis of magnetization. Then, the presence of anisotropy promotes a collinear structure over a noncollinear one which is the case here where at high temperature an amplitude-modulated collinear sinusoidal structure is preferred. Furthermore, the magnetic structures refined in both phases present an easy-axis direction in the (a, c) plane, almost perpendicular to c^* , with a robust direction with respect to temperature variations. Planar single-ion anisotropy was introduced in the spin-wave calculation to stabilize the cycloid structure in the observed plane. The observed anisotropy is significant since in a purely ionic description manganese in $\text{SrMnGe}_2\text{O}_6$ is an S -state Mn^{2+} ion with vanishing orbital moment. However it has been reported that single-ion anisotropy of Mn^{2+} cannot be neglected and plays an important role [36].

Having established the microscopic magnetism model and the driving factors stabilizing the polar elliptical cycloidal magnetic phase in $\text{SrMnGe}_2\text{O}_6$, let us now discuss in detail the direction of the electric polarization in the (ac) plane and the mechanism that can be proposed to generate it. We have measured a polarization along the a and c^* directions with almost the same amplitude, which gives a resultant experimental polarization P_{exp} with an angle of $\sim 45^\circ$ with respect to the a direction in the (ac) plane (see Fig. 10). In the well-known spin current [1] and inverse DM theories [2,37], for two adjacent spins S_i and S_j separated by the vector e_{ij} the polarization is expressed by $P_1 \propto e_{ij} \times (S_i \times S_j)$, and is therefore lying along the direction given by α . These mechanisms cannot therefore explain fully the observed polarization. We have to invoke also a polarization parallel to the cross product $P_2 \propto S_i \times S_j$, via the extended inverse DM effect proposed by Kaplan and Mahanti [6]. It is indeed allowed by symmetry because there is neither a mirror plane containing e_{ij} nor an n -fold rotation axis perpendicular to e_{ij} . Finally, in $\text{SrMnGe}_2\text{O}_6$, the induced macroscopic polarization can be understood in terms of the inverse Dzyaloshinskii-Moriya interaction combining the two orthogonal components P_1 and P_2 . This combination was found also in other spin-

driven multiferroics like in delafossite AgFeO_2 [38] or in $\text{RbFe}(\text{MoO}_4)_2$ [39].

V. CONCLUSION

In summary, we have performed a comprehensive study of multiferroic properties of $\text{SrMnGe}_2\text{O}_6$. We found two successive incommensurate spin structures below 4.36(2) and 4.05(2) K. A nonpolar amplitude-modulated collinear sinusoidal magnetic structure emerges followed by a polar elliptical cycloidal spin structure. Extended Dzyaloshinskii-Moriya mechanism successfully explains the appearance of a spontaneous polarization measured within the (ac) plane associated with the latter magnetic symmetry. The good adequacy between the determined magnetic model, the calculated magnetic phase diagram, and the measured and simulated spin wave demonstrates that the magnetic behavior of $\text{SrMnGe}_2\text{O}_6$ is well captured by a rather simple model with three competing isotropic interactions and a weak single-ion anisotropy.

ACKNOWLEDGMENTS

This work was financially supported by ANR Grant No. ANR-13-BS04-0013. We acknowledge J. Debray, A. Hadj-Azzem, and J. Balay for their help in the preparation of the samples and A. Cano for fruitful discussions. We gratefully acknowledge the Fédération Française de la Neutronique (2FDN) and Institut Laue Langevin (ILL) (Grenoble, France) for beam time access to the fabulous D23. L.D. acknowledges support from the Rutherford International Fellowship Programme (RIFP). This project has received funding from the European Union's Horizon 2020 research and innovation program under Marie Skłodowska-Curie Grant Agreement No. 665593 awarded to the Science and Technology Facilities Council.

APPENDIX: ANALYSIS OF INS DATA

As explained in the main text, the numerical approach described in this study is based on the following Hamiltonian:

$$H = J \sum_{i,j}^{\text{in chain}} S_i S_j + J_1 \sum_{i,j}^{\text{inter chain}} S_i S_j + J_2 \sum_{i,j}^{\text{inter chain}} S_i S_j + \sum_i B_{i,20} \vartheta_{i,20}.$$

In addition, to the J , J_1 , and J_2 terms, a single-ion anisotropy is taken into account, modeled by a $B_{20}O_{20}$ term, with $O_{20} = 3/2S_z^2 - 5/2(5/2 + 1)I$. This operator is written with respect to a local “ z ” quantification axis, along the $(-0.33, 0, 1)$ vector. B_{20} is positive to ensure that the spins lie in the plane perpendicular to this axis, and stabilize the cycloid structure, as inferred from diffraction. Meanwhile, the spin-wave theory is a theory of harmonic deviations of the spins around a mean-field solution. At the level of this approximation, the incommensurate propagation vector k_y and the $\Delta\Phi$ phase shift are related via the formula

$$\frac{J_1}{|J|} = -\frac{\sin(k_y + \Delta\Phi)}{\sin(\frac{k_y}{2} + \Delta\Phi)}, \quad \frac{J_2}{|J|} = -\frac{\sin(k_y + \Delta\Phi)}{2 \sin(\frac{k_y}{2})}.$$

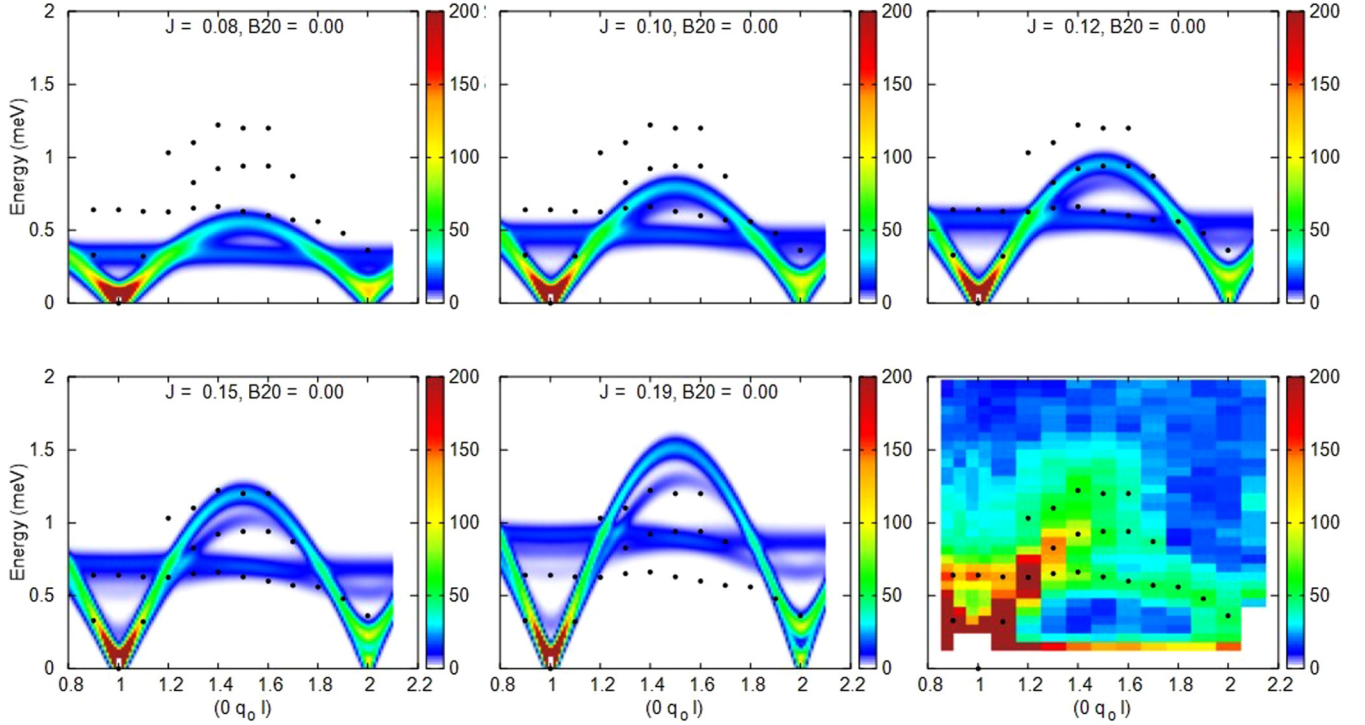


FIG. 11. Neutron intensity calculated along $(0, q_0, 1)$ for various J while $B_{20} = 0$. The bottom right panel shows the experimental data. Black dot correspond to the fitted positions of the different modes.

Diffraction measurements carried out in $\text{SrMnGe}_2\text{O}_6$ at 2 K yield $k_y = 0.424(1)$, $\Delta\Phi = 62.8(2)^\circ$, hence $J_1/|J| = 0.88(2)$ and $J_2/|J| = 0.29(1)$. Provided our minimal model is correct, these measurements thus put severe constraints on the uncertainties relative to $J_1/|J|$ and $J_2/|J|$. The values of J and B_{20} have yet to be determined.

To this end, a series of calculations has been carried out keeping the ratios $J_1/|J|$ and $J_2/|J|$ constant, but varying J and B_{20} in a systematic way. We have considered $0.05 < J < 0.19$ meV and $0 < B_{20} < 0.42$ meV. At the same time, we compared the Curie-Weiss temperature value predicted by the calculation to the experimental value, equal to 20 K.

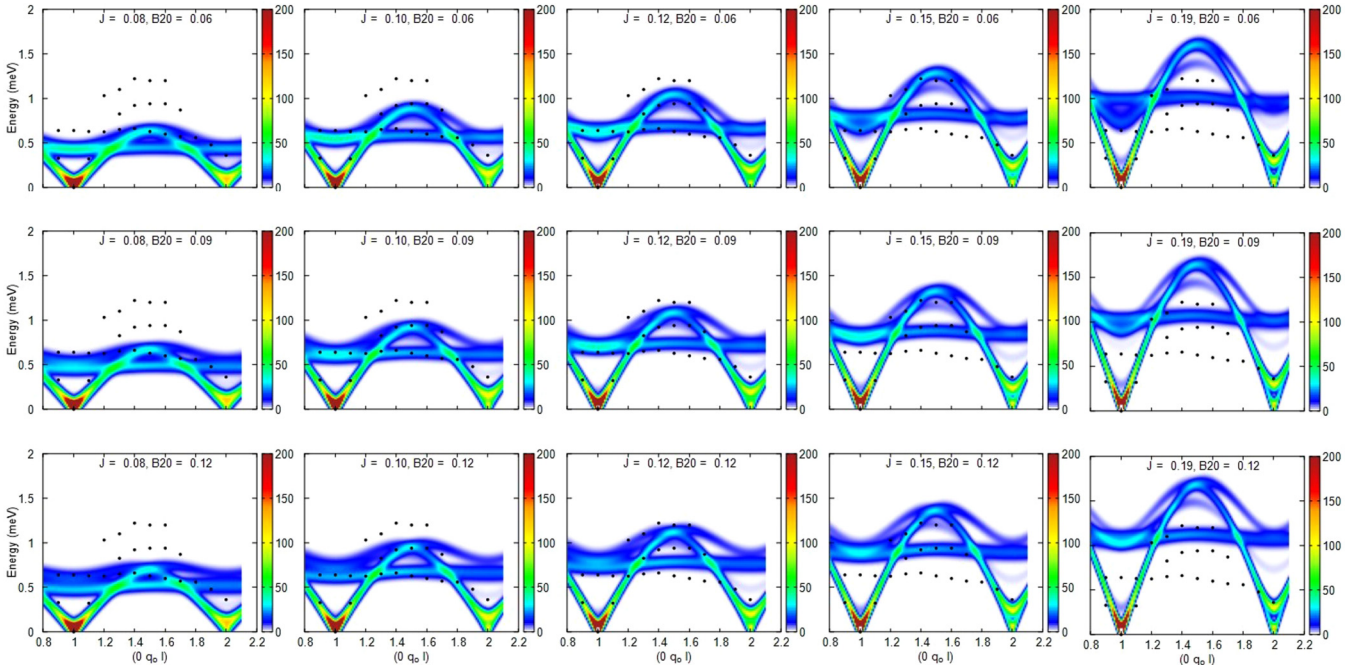


FIG. 12. Neutron intensity calculated along $(0, q_0, 1)$ for various J and B_{20} .

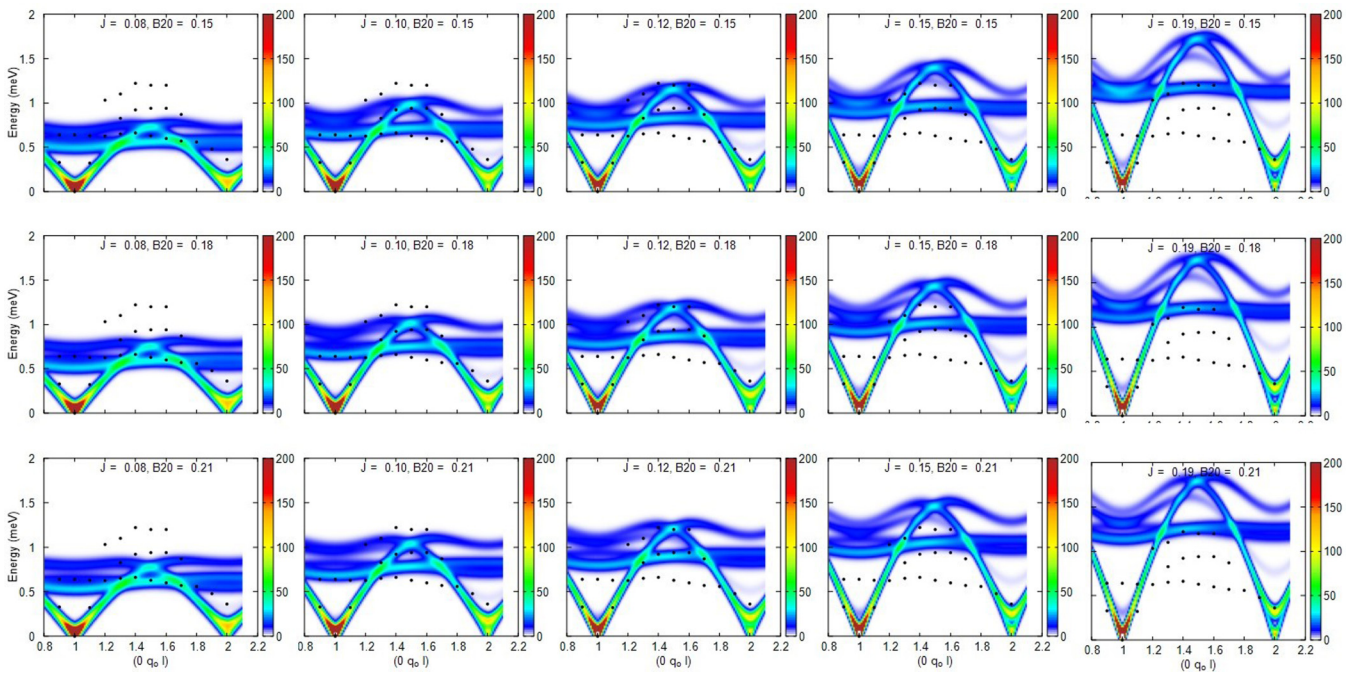


FIG. 13. Neutron intensity calculated along $(0, q_0, 1)$ for various J and B_{20} .

The main results are reproduced in Figs. 11–14. These figures display the neutron intensity calculated along $(0q_0 1)$ and $(0k 1)$, as well as the measured energies of the modes based on standard fits to the experimental data (see the black dots in the figures). The full experimental data are also reproduced for a more convenient comparison. These calculations show relatively good agreement for $0.1 < J < 0.12$ meV with $0.06 < B_{20} < 0.18$ meV. More precisely, best values are found for

$J = 0.1$ meV, $B_{20} = 0.15$, and, if $J = 0.12$, we get $B_{20} = 0.09$ meV. This indicates a correlation between J and B_{20} , estimated to be $B_{20} \sim -3(J - 0.1) + 0.15$. According to this analysis, we thus have

$$J = 0.11 + / - 0.01 \text{ meV} \quad \text{and} \quad B_{20} \sim -3(J - 0.1) + 0.15, \text{ i.e., and } \delta B_{20} \sim 3\delta J.$$

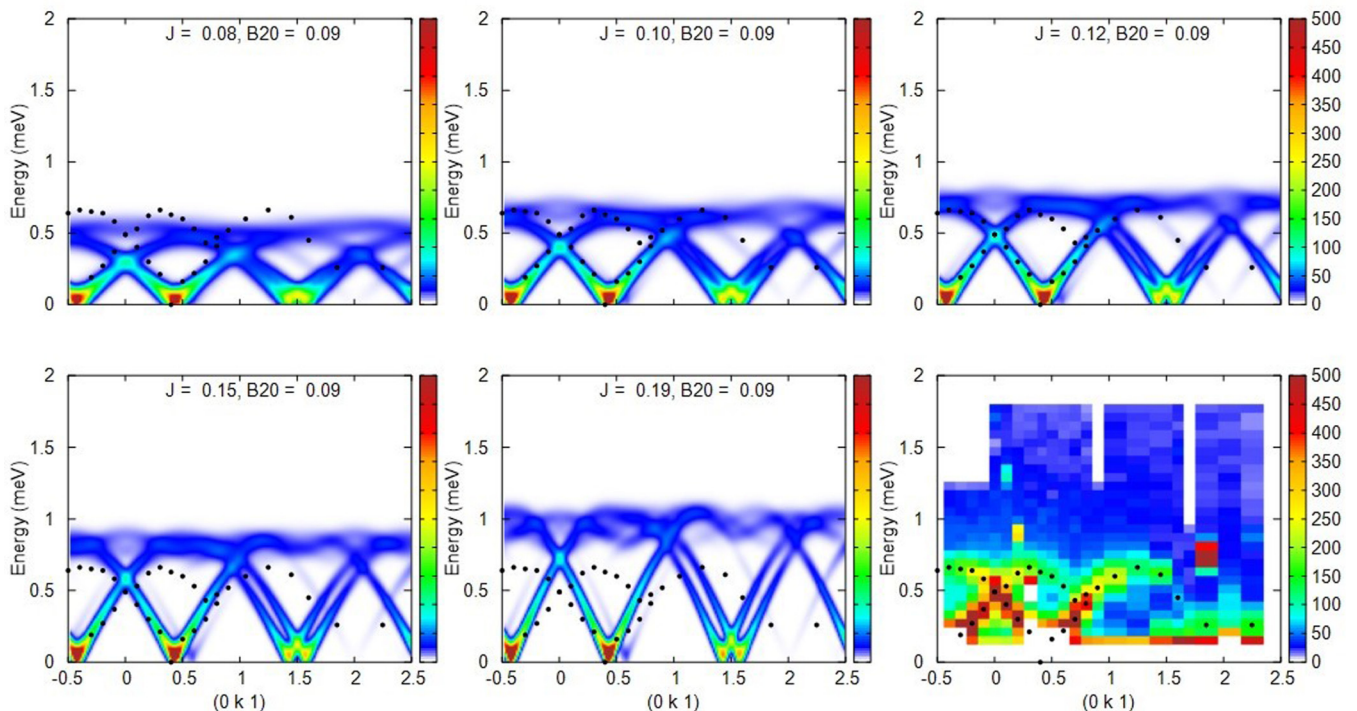


FIG. 14. Neutron intensity calculated along $(0, k, 1)$ for various J and $B_{20} = 0.09$ meV. The bottom right panel shows the experimental data.

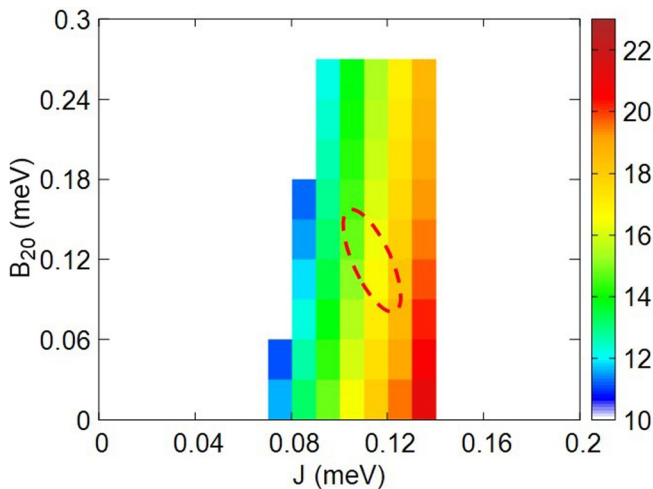


FIG. 15. Curie-Weiss temperature (in K; see the color scale on the right of the figure). The dashed ellipse shows the range of parameters determined by comparison with INS data. Since the experimental Curie-Weiss temperature is 20 K, this cross-check calculation favors the strongest values of J .

Figure 14 displays part of the calculations performed for the $(0\ k\ 1)$ direction. They confirm the relatively good agreement for the range of parameters determined above.

Figure 15 shows the Curie-Weiss temperature calculated in the (J, B_{20}) range of interest. The comparison with the experimental value is quite good, hence giving some more confidence in the analysis. Since the experimental Curie-Weiss temperature is 20 K, this cross-check calculation would favor the strongest values of J , hence $J = 0.12$ meV, $B_{20} = 0.09$ meV.

We also should stress that in incommensurate magnets, in-plane and out-of-plane modes are expected. In-plane modes correspond to correlations between spin components within the spiral plane. In the long-wavelength limit, they correspond to a global phase shift of the spins. These are the Goldstone mode of the model, and soften down to zero energy at the magnetic Bragg peaks. Importantly, the planar anisotropy term B_{20} does not induce any spin gap for them since the spins keep an overall degree of rotation in the easy plane. In contrast, Figs. 11–14 show that B_{20} affects quite strongly the high-energy part of the spectrum.

We anticipate, however, that measurements in other directions are likely necessary to come to a definitive conclusion and propose a better model.

- [1] H. Katsura, N. Nagaosa, and A. V. Balatsky, *Phys. Rev. Lett.* **95**, 057205 (2005).
- [2] I. A. Sergienko and E. Dagotto, *Phys. Rev. B* **73**, 094434 (2006).
- [3] T. H. Arima, *J. Phys. Soc. Jpn.* **76**, 073702 (2007).
- [4] M. Kenzelmann, A. B. Harris, S. Jonas, C. Broholm, J. Schefer, S. B. Kim, C. L. Zhang, S. W. Cheong, O. P. Vajk, and J. W. Lynn, *Phys. Rev. Lett.* **95**, 087206 (2005).
- [5] Y. Yamasaki, S. Miyasaka, Y. Kaneko, J.-P. He, T. Arima, and Y. Tokura, *Phys. Rev. Lett.* **96**, 207204 (2006).
- [6] T. A. Kaplan and S. D. Mahanti, *Phys. Rev. B* **83**, 174432 (2011).
- [7] S. Jodlauk, P. Becker, J. A. Mydosh, D. I. Khomskii, T. Lorenz, S. V. Streltsov, D. C. Hezel, L. Bohat, L. Bohatý, L. Bohaty, and L. Bohat, *J. Phys.: Condens. Matter* **19**, 432201 (2007).
- [8] S. V. Streltsov, J. McLeod, A. Moewes, G. J. Redhammer, and E. Z. Kurmaev, *Phys. Rev. B* **81**, 045118 (2010).
- [9] G. J. Redhammer, A. Senyshyn, M. Meven, G. Roth, S. Prinz, A. Pachler, G. Tippelt, C. Pietzonka, W. Treutmann, M. Hoelzel, B. Pedersen, and G. Amthauer, *Phys. Chem. Miner.* **38**, 139 (2011).
- [10] M. Baum, A. C. Komarek, S. Holbein, M. T. Fernández-Díaz, G. André, A. Hiess, Y. Sidis, P. Steffens, P. Becker, L. Bohatý, and M. Braden, *Phys. Rev. B* **91**, 214415 (2015).
- [11] I. Kim, B.-G. Jeon, D. Patil, S. Patil, G. Nénert, and K. H. Kim, *J. Phys.: Condens. Matter* **24**, 306001 (2012).
- [12] M. Ackermann, L. Andersen, T. Lorenz, L. Bohatý, and P. Becker, *New J. Phys.* **17**, 13045 (2015).
- [13] T. Drokina, G. Petrákovskii, L. Keller, and J. Schefer, *J. Phys. Conf. Ser.* **251**, 012016 (2010).
- [14] L. Ding, P. Manuel, D. D. Khalyavin, F. Orlandi, and A. A. Tsirlin, *Phys. Rev. B* **98**, 094416 (2018).
- [15] C. Lee, J. Kang, J. Hong, J. H. Shim, and M.-H. Whangbo, *Chem. Mater.* **26**, 1745 (2014).
- [16] P. J. Baker, H. J. Lewtas, S. J. Blundell, T. Lancaster, I. Franke, W. Hayes, F. L. Pratt, L. Bohatý, and P. Becker, *Phys. Rev. B* **81**, 214403 (2010).
- [17] G. Nénert, M. Isobe, C. Ritter, O. Isnard, A. N. Vasiliev, and Y. Ueda, *Phys. Rev. B* **79**, 064416 (2009).
- [18] G. Nénert, M. Isobe, I. Kim, C. Ritter, C. V. Colin, A. N. Vasiliev, K. H. Kim, and Y. Ueda, *Phys. Rev. B* **82**, 024429 (2010).
- [19] O. Janson, G. Nénert, M. Isobe, Y. Skourski, Y. Ueda, H. Rosner, and A. A. Tsirlin, *Phys. Rev. B* **90**, 214424 (2014).
- [20] L. Ding, C. V. Colin, C. Darie, J. Robert, F. Gay, and P. Bordet, *Phys. Rev. B* **93**, 064423 (2016).
- [21] S. V. Streltsov and D. I. Khomskii, *Phys. Rev. B* **77**, 064405 (2008).
- [22] L. Ding, C. V. Colin, C. Darie, and P. Bordet, *J. Mater. Chem. C* **4**, 4236 (2016).
- [23] J. Rodríguez-Carvajal, *Phys. B* **192**, 55 (1993).
- [24] P. J. Becker and P. Coppens, *Acta Crystallogr. Sect. A* **30**, 129 (1974).
- [25] H. T. Stokes, D. M. Hatch, and B. J. Campbell, ISOTROPY Software Suite, Iso.Byu.Edu.
- [26] J. M. Perez-Mato, S. V. V Gallego, E. S. S. Tasci, L. Elcoro, G. De Flor, M. I. I. Aroyo, G. de la Flor, and M. I. I. Aroyo, *Annu. Rev. Mater. Res.* **45**, 217 (2015).
- [27] W. H. Baur, *Acta Crystallogr. Sect. B* **30**, 1195 (1974).
- [28] J. M. Perez-Mato, J. L. Ribeiro, V. Petricek, and M. I. Aroyo, *J. Phys.: Condens. Matter* **24**, 163201 (2012).
- [29] In the spin context isotropy means “the same in all directions” in “spin-space.” That is, an isotropic exchange interaction is

- one where the x components of the two spins interact the same as the y components, and both interact the same as the z components. For two spin, the isotropic interaction is the Heisenberg interaction ($\vec{S} \cdot \vec{S}$).
- [30] T. A. Kaplan and N. Menyuk, *Philos. Mag.* **87**, 3711 (2007).
- [31] G. Nénert, C. Ritter, M. Isobe, O. Isnard, a. Vasiliev, and Y. Ueda, *Phys. Rev. B* **80**, 024402 (2009).
- [32] G. Nénert, I. Kim, M. Isobe, C. Ritter, A. N. Vasiliev, K. H. Kim, and Y. Ueda, *Phys. Rev. B* **81**, 184408 (2010).
- [33] G. J. Redhammer, G. Roth, W. Treutmann, W. Paulus, G. André, C. Pietzonka, and G. Amthauer, *J. Solid State Chem.* **181**, 3163 (2008).
- [34] S. Petit, *Collect. SFN* **12**, 105 (2011).
- [35] F. V. Temnikov, E. V. Komleva, Z. V. Pchelkina, and S. V. Streltsov, *JETP Lett.* **110**, 595 (2019).
- [36] E. Ressouche, M. Loire, V. Simonet, R. Ballou, A. Stunault, and A. Wildes, *Phys. Rev. B* **82**, 100408(R) (2010).
- [37] M. Mostovoy, *Phys. Rev. Lett.* **96**, 067601 (2006).
- [38] N. Terada, D. D. Khalyavin, P. Manuel, Y. Tsujimoto, K. Knight, P. G. Radaelli, H. S. Suzuki, and H. Kitazawa, *Phys. Rev. Lett.* **109**, 097203 (2012).
- [39] J. S. White, C. Niedermayer, G. Gasparovic, C. Broholm, J. M. S. Park, A. Y. Shapiro, L. A. Demianets, and M. Kenzelmann, *Phys. Rev. B* **88**, 060409(R) (2013).